Structural Confinement Effects of an Amorphous Magneto-Semiconductor within Nanochannels

Weon-Sik Chae,[a] Kyoung-Hoon Choi,[a] Yong-Rok Kim,[a]* Jin-Seung Jung,[b]*
Leszek Malkinski[c] and Charles J. O'Connor[c]
[a]*Photon Applied Functional Molecule Research Laboratory, Department of Chemistry, Yonsei University, Seoul 120-749, South Korea*
[b]*Department of Chemistry, Kangnung National University, Kangnung 210-702, South Korea*
[c]*Advanced Material Research Institute, University of New Orleans, LA 70148, USA*

Optical and magnetic properties have been investigated for the structurally confined amorphous magneto-semiconductor, ternary chalcogenide, within the nanochannels of the mesoporous host. The structural confinement induced a weak crystallographic ordering of the magneto-semiconductor within the nanochannels. Unique optical properties were observed for this nanocomposite, which were possibly due to the size and energy quantization of the confined guest chalcogenide within the nanochannels. The structural confinement also induced the suppression of the phonon coupling to the photoexcited carriers during the carriers' recombination process. The spin-glass freezing temperature (T_f = 4.2 K) which was the characteristic magnetic transition temperature for the amorphous bulk was shifted to 2.3 K for the confined system, possibly due to the generation of the superparamagnetic domains induced by the quantum confinement effect.

Keywords: Magneto-semiconductor; Chalcogenide; Mesoporous; Exciton recombination; Spin-glass.

INTRODUCTION

In the field of nano-science and technology, the precision controls of size and shape and the maintenance of the nanostructure are important research subjects for providing specific and stable nanoproperties. For these purposes, nanotemplating has been suggested as one promising method.[1-3] Recently, various mesoporous materials have been utilized as templating nanomolds for nanocomposites and free-standing nanomaterials, which can provide stable and highly-ordered nanostructures.[4-10] To date, several different types of mesoporous materials have been fabricated to have the various porous structures which have controlled pore diameters,[11,12] variable compositions,[13-17] and designed morphologies.[18-23] Such utilization of mesoporous templates have produced unique nanomaterials of semiconductors, metals, magnets, and organic compounds, and which present interesting nano-chemical and physical properties.[23-31]

As one of the quantum confined systems, the semiconductor quantum dot has been investigated intensively due to its tunable band-gap property of quantum size effect. However, the bare semiconductor quantum dots typically have a wide range of emissions which originate from several recombination pathways such as direct band-to-band recombination, shallow-trapped recombination, and deep-trapped recombination in surface defects, etc. Especially, the precision control of the emissions originating from the surface defect states is somewhat difficult due to the complex bonding nature on the surface of the quantum dot. Recently, mesoporous materials have been utilized as templates for the emission control which is induced by the structural confinement of the semiconductor quantum dots.[24,32,33] The previous studies suggest that the surface state emission could be removed by the selective elimination of the surface defect sites with the functionalized mesoporous nanochannels, which provide the controllable direct excitonic emission induced by unique nanopatterned

Special Issue for the 4th Asia Photochemistry Conference, January 5~10, 2005, Taipei, Taiwan, R.O.C.
* Corresponding author. E-mail: yrkim@yonsei.ac.kr and jjscm@kangnung.ac.kr

morphologies.[32,33]

Although the various fabrication methodologies have continuously been developed for structurally confined nanocomposite systems, controlled studies of the energetic properties are limited to a few trials for the nanocomposite systems including the monofunctional materials such as semiconductors[24,32,33] and organic compounds.[29-31] Since the magneto-semiconductors show multiple responses depending on the applied optical and/or magnetic fields,[34,35] they can be utilized to be potential materials for multifunctional nanodevices. Therefore, in this study, the amorphous magneto-semiconductor is incorporated into the nanochannels of the mesoporous host template in order to investigate the unique optical and magnetic properties which are possibly induced by the confinement within the long-range ordered nanochannels. From the study, it is observed that the structural nano-confinement appears to induce unique physical properties such as enhanced crystallinity, suppressed phonon coupling, and superparamagnetic coupling in the controlled nanodomain of the magneto-semiconductor confined within the mesoporous host nanochannels.

EXPERIMENTAL

Preparation

The magneto-semiconductor of the ternary chalcogenide, $Co_3(SbTe_3)_2$, was prepared from the metathesis reaction between cobalt(II) chloride and the Zintl phase precursor of K_3SbTe_3 in polar solvent.[35] The fast precipitation reaction resulted in an amorphous structure which showed the magnetically interesting spin-glass behavior at the extremely low temperature of 4.2 K.[34,35]

The brief incorporation strategy of the guest $Co_3(SbTe_3)_2$ into a mesoporous host was as follows: Initially, divalent cobalt ions were deposited within the mesoporous nanochannels through electrostatic interactions, and the subsequent rapid precipitation with the injected K_3SbTe_3 precursor produced ternary chalcogenide within the nanochannels. For the efficient loading of the guest chalcogenide within the mesoporous host, the negatively charged aluminosilicate of AlMCM-41 (with MCM-41 structure; typical Si/Al ratio was 7-14[4,27]) was utilized as the mesoporous host template due to the enhanced ion-exchange capacity: Since the aluminum substituted silica framework exhibited a negative charge, its ion-uptake capacity was enhanced compared with the pure siliceous MCM-41 of which the nanochannel surface was typically covered with the hydroxyl groups.

In this study, the utilized mesoporous host of the AlMCM-41 was prepared by following previous reports.[4,27] The Zintl phase precursor of K_3SbTe_3 was synthesized by the solid state reaction of the respective elements in a sealed quartz tube at the temperature of 550 °C.[36] Anhydrous cobalt(II) chloride (98%, Aldrich) was used as received.

As the fabricated host of the AlMCM-41 (0.2 g) was mixed with 20 mL of 0.05 M cobalt(II) chloride aqueous solution, the cobalt(II) ions were preferentially exchanged with the Na(I) ions which initially existed at the wall surface of the host nanochannels. This ion exchange process was repeatedly accomplished three times to have the increased loading amount of the cobalt ions, similar to the methods of the metal loading within the AlMCM-41.[4,27,37] The resulting pale pink powder of the Co(II) ion exchanged AlMCM-41 (Co^{2+}-AlMCM-41) was suspended in the purified deoxygenated water for 1 hour in order to remove the cobalt(II) ions adsorbed on the external surface of the mesoporous host microparticles.[37] After the evacuation of water from the Co^{2+}-AlMCM-41, the addition of 20 mL of 0.05 M K_3SbTe_3 aqueous solution to the Co^{2+}-AlMCM-41 resulted, through in part the capillary action and the precipitation reaction within the nanochannels, in the gray colored powder of the nanocomposite: $Co_3(SbTe_3)_2$ incorporated within the AlMCM-41. The residual ionic species were removed by repetitive washing with the purified deoxygenated water and subsequently dried at 60 °C in an oven overnight. Due to the air sensitivity of the guest ternary chalcogenide, all chemical processes were carried out in a glove box and the conventional Schlenk tubes filled with argon gas. The final powder product is hereafter denoted as CST@AlMCM.

Structural Characterization

Quantitative analysis for the CST@AlMCM nanocomposite was performed by an atomic absorption spectroscope (Perkin-Elmer AA100), which indicated that the contents of the ternary chalcogenide loaded within the nanochannels of the AlMCM-41 host was 4.5 wt.-%. Since the bulk chalcogenide was not detected at the surface of the AlMCM-41 host from transmission electron microscope (TEM) images, this loading amount was assigned to the incorporated guest chalcogenide. For the structural informa-

tion on the mesoporous host and the CST@AlMCM nanocomposite, powder X-ray diffraction (XRD) data were collected with a Philips X'Pert MPD system with copper radiation (λ = 1.5418 Å), and TEM images were obtained with a Philips CM-20 system operated at 200 kV for the samples that were deposited on the carbon-coated copper grids. Nitrogen adsorption measurements were carried out by using an adsorption analyzer (Micromeritics ASAP 2010). Before the measurements, all samples were degassed for 2 hours at 473 K under the vacuum of $\sim 10^{-3}$ Torr.

Optical and Magnetic Characterizations

For the powder-type bulk $Co_3(SbTe_3)_2$ and the CST@AlMCM nanocomposite, steady-state photoluminescence (PL) and excitation (PLE) spectra were measured with a fluorimeter (Hitachi F-4500). Low temperature PL measurement at 77 K was conducted in a Dewar vessel cell containing liquid nitrogen. A picosecond time-correlated single photon counting (TCSPC) system was employed for the time-resolved PL decay measurements. Details of the laser system and the fitting routine are described in previous reports.[38,39] The PL, PLE, and PL lifetimes were measured at the front face of the powder samples in a sealed quartz cuvette filled with argon gas. DC magnetic susceptibility measurements in both field-cooled (FC) and zero-field-cooled (ZFC) conditions were performed with a function of temperature down to 2 K by utilizing a magnetometer (SQUID, Quantum Design MPMS-5S). The calibration and measurement procedures have been described in previous reports.[40]

RESULTS AND DISCUSSION

Structural characteristics

Fig. 1 shows the powder XRD patterns for the mesoporous AlMCM-41 host and the CST@AlMCM nanocomposite in the small- and the wide-angle regions. For the mesoporous host, three diffraction peaks are clearly observed in the small-angle region, which can be assigned to the (100), (110), and (200) planes of the hexagonal mesostructure. For the CST@AlMCM nanocomposite, the characteristic diffraction peaks are shown to be decreased in their intensities and slightly shifted to the high-angle compared with those of the empty host. It implies that the guest chalcogenide is incorporated within the nanochannels of the mesoporous host: The incorporated guest often reduces the diffractional contrast between the porous channel and the wall framework of the mesoporous materials.[5,6,33] Moreover, it is noteworthy that the incorporated guest chalcogenide within the AlMCM-41 host presents weak diffraction peaks at 17.7°, 27.5°, and 31.4° in 2θ (indicated by asterisks) where the mesoporous host and the amorphous bulk guest show only broad diffraction patterns in this wide-angle region (inset of Fig. 1). Therefore, such newly observed diffractions imply that the guest chalcogenide has an enhanced crystallographic ordering within the long-range ordered nanochannels of the AlMCM-41 host due to the nano-confinement effect.

For the AlMCM-41 host template, the characteristic hexagonal mesoporous structure and the long-range ordered nanochannel array are shown well in the TEM images (Fig. 2a and b). Such mesoporous structures are also well conserved in the CST@AlMCM nanocomposite which includes the guest chalcogenide, although the image contrast between the nanochannels and the wall framework is somewhat reduced compared with the empty host. Since the incorporated heavy metal compounds can reduce the density contrast between the pore and the wall of the mesoporous structure, as mentioned in the experimental section of the XRD study, the reduced image contrast in the CST@AlMCM can be due to the filling effect of the heavy atomic guest chalcogenide inside the mesoporous nanochannels (Fig. 2c

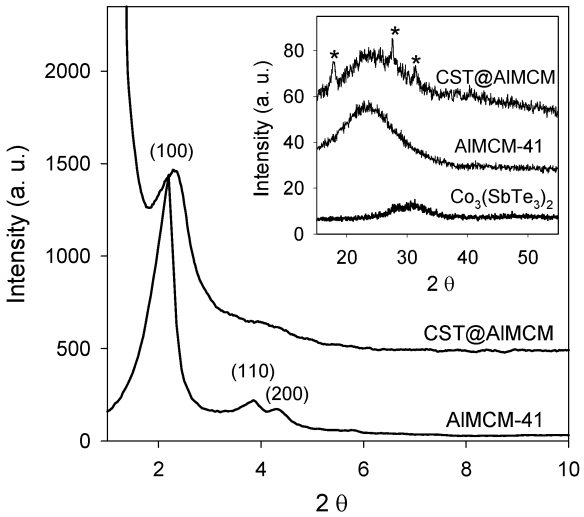

Fig. 1. Powder X-ray diffractions for the AlMCM-41 host and the CST@AlMCM nanocomposite in the small-angle region. The inset is the X-ray diffractions in the wide-angle region for the bulk $Co_3(SbTe_3)_2$, the host, and the nanocomposite.

and d).

Fig. 3 shows the nitrogen adsorption-desorption isotherms for the empty mesoporous host and the CST@AlMCM nanocomposite. The Brunauer-Emmett-Teller (BET) surface area and the pore volume are estimated to be 636 m^2/g and 0.56 cm^3/g for the empty host, respectively. For the CST@AlMCM nanocomposite, the BET surface area and the pore volume are reduced to 444 m^2/g and 0.28 cm^3/g, respectively. The reduction of the surface area and the pore volume indicates that the guest chalcogenide is incorporated inside of the mesoporous AlMCM-41 nanochannels, which is consistent with the results from the XRD and the TEM studies.

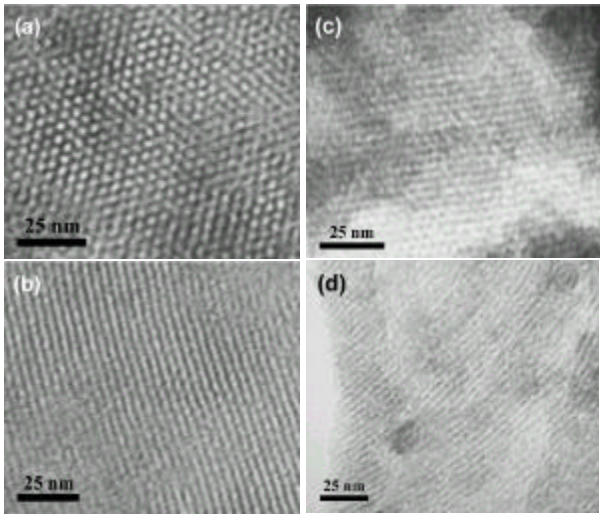

Fig. 2. TEM images for (a and b) the AlMCM-41 host and (c and d) the CST@AlMCM nanocomposite at the parallel (hexagonal) and the perpendicular (lamellar) directions to the pore opening.

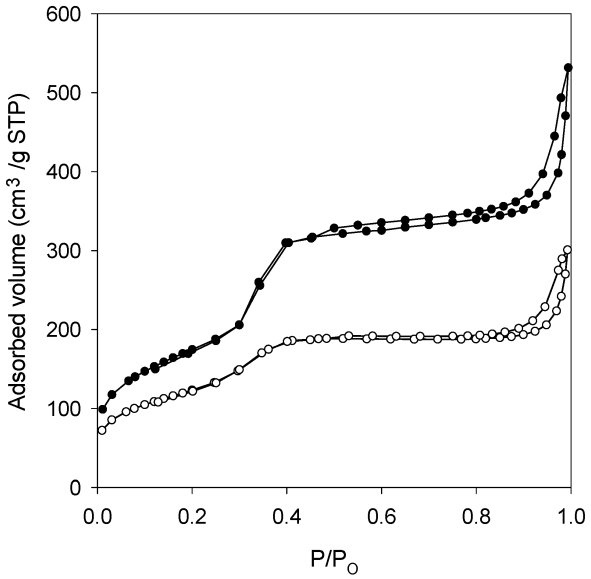

Fig. 3. Nitrogen adsorption-desorption isotherms for the AlMCM-41 host (closed circle) and the CST@AlMCM nanocomposite (open circle).

Optical properties

The amorphous bulk magneto-semiconductor, $Co_3(SbTe_3)_2$, shows the excitation onset at ~ 310 nm. The emission spectrum for the amorphous bulk exhibits the broad spectral range centered at ~ 450 nm at room temperature (RT), which is largely Stokes-shifted from the excitation onset (Fig. 4a). Such emission characteristics of the

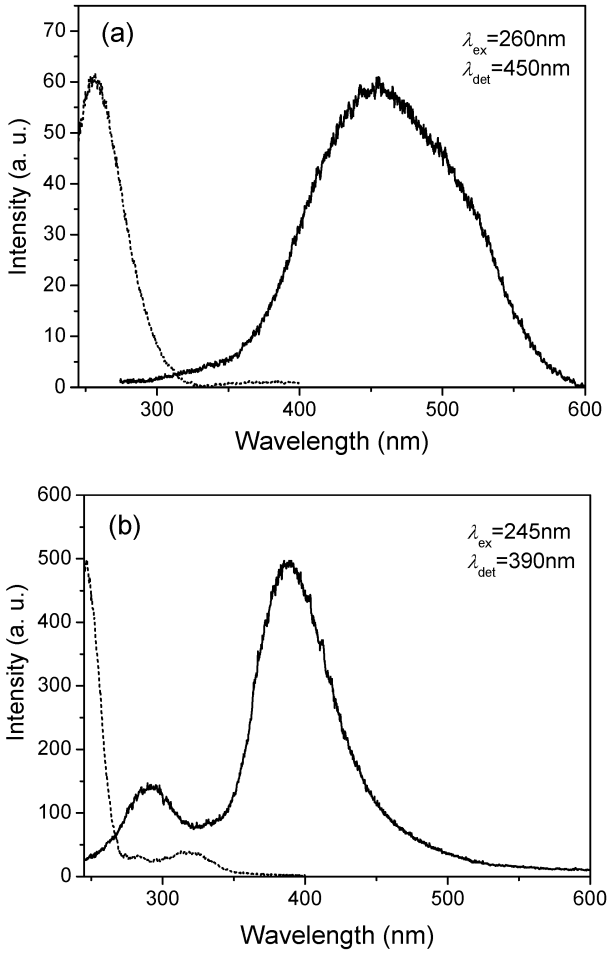

Fig. 4. PL (solid line) and PLE (dotted line) spectra for (a) the amorphous bulk $Co_3(SbTe_3)_2$ and (b) the CST@AlMCM nanocomposite at room temperature. λ_{ex} and λ_{det} indicate the excitation wavelength for the PL and the detection wavelength for the PLE, respectively.

large Stokes-shift most probably originates from the small polaron states existing in the amorphous structure of the bulk chalcogenide: The existence of the small polaron states was suggested for the amorphous local structures of which the excited states had a strong tendency to lower their potential energies by deforming the surrounding network[41,42] and, therefore, generated the deep-trapped potential states below the band-gap energy.[38]

The aluminosilicate mesoporous material (AlMCM-41) that is used as a host for the incorporation of the ternary chalcogenide may have several defect sites within its wall framework. Typically, these defect sites induce the weak broad emission centered at 420 nm and extended to 600 nm.[38] Since the AlMCM-41 utilized in this study are obtained from the same synthetic batch which has been utilized for the previous studies,[38,44] the AlMCM-41 in this study are expected to have similar emission characteristics with the previous studies which indicate that the emission intensity of the mesoporous host is not prominent at all. Therefore, based on the reported emission intensity and spectral range of AlMCM-41,[38] the observed PL and PLE spectra (Fig. 4b, 5) are considered to represent the spectral properties of the confined guests in the nanocomposite systems.

For the CST@AlMCM nanocomposite, the excitation spectrum is dominantly located in the range shorter than ~ 270 nm as shown in Fig. 4b. The major excitation band for the nanocomposite, which is blue-shifted from the excitation onset of the amorphous bulk, possibly comes from the quantum size effects of the confined guest chalcogenide within the nanochannels of the AlMCM-41 host. Moreover, a weak electronic transition is additionally observed at ~ 320 nm below the band-to-band transition at ~ 270 nm. Previously, an indirect electronic absorption below the interband transition was also observed in the small semiconductor quantum dot, which was assigned to the electronic transition induced by the surface states.[43] Similarly, from our previous study for the confined chalcogenide within a mesoporous host, it was also suggested that the newly observed electronic transitions below the bulk band-gap energy might be induced by a strong coupling between the guest and the host wall framework.[44] Therefore, it is considered that the weak excitation band at ~ 320 nm in the CST@AlMCM nanocomposite is possibly ascribed to the indirect electronic transition involving the potential energy state generated by a strong coupling in the interface region between the confined guest chalcogenide and the wall framework of the AlMCM-41 host.

As well as the changes of the excitation spectrum, the CST@AlMCM nanocomposite shows two distinctive emission spectral features: The intense emission peak is blue-shifted from ~ 450 nm to ~ 390 nm and narrowed compared with the emission of the amorphous bulk. Another interesting feature is that a weak band-edge emission is additionally observed at ~ 290 nm (Fig. 4b). The blue-shifted and narrowed emission band is possibly due to the size and energy quantization of the confined guest chalcogenide within the nanochannels with a diameter of ~ 3.6 nm (estimated from the BET and TEM measurements). In order to reveal the origin of the newly observed band-edge emission at ~ 290 nm for the CST@AlMCM nanocomposite, the emission spectrum was measured at the low temperature of 77 K (Fig. 5). Interestingly, the emission spectrum measured at 77 K shows that the band-edge emission is largely enhanced in its intensity and blue-shifted to 286 nm from the band-edge emission (290 nm) measured at RT.

In general, it is well known that the photoexcited carriers in conduction band or shallow-trapped states are rapidly trapped to the deep-trapped states through phonon coupling.[45] Therefore, the phonon-mediated carriers' recombination process in the deep-trapped states can be the dominant recombination process at high temperature. On the

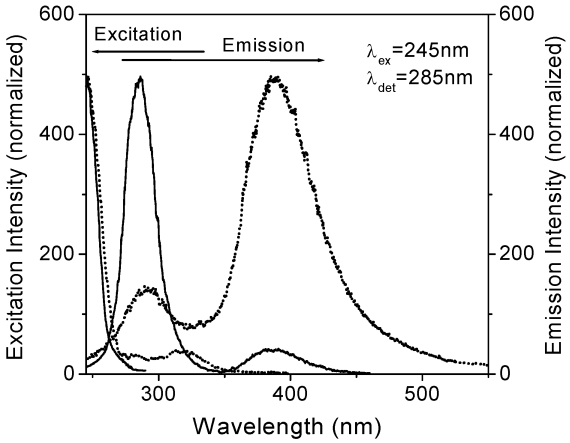

Fig. 5. PL and PLE spectra for the CST@AlMCM nanocomposite at 77 K (solid lines). λ_{ex} and λ_{det} indicate the excitation wavelength for the PL and the detection wavelength for the PLE, respectively. The PL and PLE spectra measured at room temperature (dotted lines) are also presented for the comparison.

other hand, it is expected for the band-edge emission to increase with the temperature reduction since the thermal energy (k_BT) coupling of the photoexcited carriers in the conduction band and/or shallow-trapped states is to be generally reduced with decreasing temperature. In particular, it was previously reported that the photoexcited carriers' recombination in the confined semiconductors within the nanospaces was experimentally proven to be less subjected to the phonon coupling than that in the bulk.[38,44,46] Based on these recombination dynamics, it is suggested that the newly observed band-edge emission in the CST@AlMCM nanocomposite occurs due to the reduced thermal effect during the recombination processes, i.e., the suppression of the phonon coupling to the photoexcited carriers generated in the nanocomposite. Such suppression of the phonon coupling possibly reduces the trapping of the photoexcited carriers from the conduction band and/or shallow trapped states to the deep-trapped states. And, therefore, it induces the band-edge emission appearing in the CST@AlMCM nanocomposite. Such possible mediation of the phonon coupling during the recombination process is also reflected in the time-resolved emission decay.

In order to study the confinement effect during the recombination process, the time-resolved emission decays were measured for the amorphous bulk state of the guest chalcogenide and the incorporated form of the CST@AlMCM nanocomposite (Fig. 6). Since the emission decays consist of the multiple lifetime components due to the complicated relaxation processes through the various potential trap states existing in both the amorphous bulk and the nanocomposite, the lifetime is presented as a mean lifetime to provide a simplified view (Table 1). Although both the measurements were similarly conducted at RT, the observed wavelength-dependent emission decays showed at least twice longer lifetimes for the CST@AlMCM than those for the amorphous bulk chalcogenide. These lengthened lifetime components of the confined guest within the mesoporous host imply that the photoexcited carriers experience less optical phonon coupling than that in the amorphous bulk at RT. The results from the time-resolved emission decays are well correlated with the expectation of the plausible suppression of the phonon coupling and the induction of the band-edge emission, as suggested from the temperature-dependent emission study.

As another possible reason for the occurrence of the band-edge emission in the CST@AlMCM, the quantum size effect of the confined guest chalcogenide within the mesoporous host can be suggested. As the particle size of the semiconductor reduces to a few nanometers, the interaction probability between the photoexcited electrons and holes is expected to increase, which may result in the enhancement of the direct recombination between the photoexcited charge carriers. In this case, the recombination rate is typically faster than the rate in the bulk.[47,48] However, the observed lengthened emission lifetimes in the CST@AlMCM nanocomposite are contrary to the expectation from the quantum size effect. Therefore, the band-edge emission observed in this nanocomposite is most probably due to the suppression of phonon coupling to the photoexcited carriers.

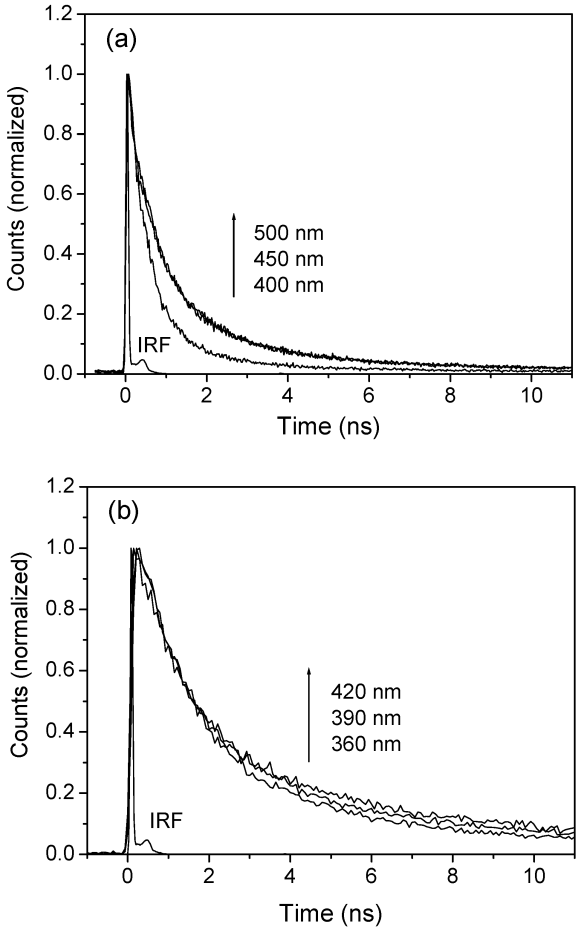

Fig. 6. Time-resolved PL decays for (a) the amorphous bulk $Co_3(SbTe_3)_2$ and (b) the CST@AlMCM nanocomposite at room temperature. The excitation wavelength is 287 nm for both the samples and the detection wavelengths are indicated in the figures. The instrumental response function (IRF) with a full width at half maximum of 67 ps is also presented.

Table 1. Wavelength dependent PL lifetimes for the amorphous bulk $Co_3(SbTe_3)_2$ and the incorporated form of the CST@AlMCM nanocomposite

Sample	λ_{det} (nm)	Lifetime (ns, $<\tau>$)	χ^2
bulk $Co_3(SbTe_3)_2$	400	0.9	1.5
	450	1.2	1.1
	500	1.2	1.4
CST@AlMCM	360	2.5	1.2
	390	2.9	1.1
	420	3.1	1.2

$I(t) = A_1 e^{-t/\tau_1} + A_2 e^{-t/\tau_2} + A_3 e^{-t/\tau_3} + \cdots$; $I(t)$ is the time-dependent PL intensity, A is the amplitude, and τ is the lifetime. The mean lifetimes are deduced as follows; $<\tau> = \sum_i A_i \tau_i^2 / \sum_i A_i \tau_i$. The excitation wavelength is 287 nm. λ_{det} represents the detection wavelengths.

Magnetic properties

It was previously reported that the bulk ternary chalcogenide of $Co_3(SbTe_3)_2$ showed the typical spin-glass behavior with the freezing temperature of 4.2 K.[34,35] In this study, the amorphous bulk ternary chalcogenide also shows the similar freezing temperature of 4.5 K with the reported value (inset of Fig. 7). As the guest chalcogenide is incorporated within the host nanochannels, several interesting magnetic properties are observed in the nanocomposite system as follows: The transition temperature for the confined guest appears at the temperature of 2.3 K which is lower than the freezing temperature of 4.5 K for the bulk. The magnetic hysteresis loop with the coercive force of 100 Oe is newly observed at 2 K. The ZFC and FC curves of the CST@AlMCM nanocomposite do not converge within the experimental temperature range of 15 K, while the ZFC and FC curves of the bulk chalcogenide overlap just above the freezing temperature.

Among the changes in the magnetic properties, it is noticeable that the newly observed magnetic hysteresis loop is not the characteristic of the spin-glass system since the spin-glass property arises from a random exchange field that is experienced by the neighbor magnetic spins in random orientation.[34] Interestingly, such a magnetic hysteresis loop is a typical pattern of the superparamagnetic property which appears below the characteristic blocking temperature.[49,50] It should also be noted that both the spin-glass materials and the superparamagnetic systems can provide the same type of temperature dependence of the magnetic susceptibility which is characterized by the maximum of the ZFC curve and the hyperbolic decay at a higher temperature than freezing (for the spin-glasses) or blocking (for the superparamagnets) temperatures.[51,52] However, the observed magnetic hysteresis loop suggests that the superparamagnetic domains are newly generated in the confined chalcogenides within the nanochannels of the host AlMCM-41. From the optical studies, the unique confinement effects such as enhanced crystallinity, size and energy quantization, and reduced thermal effect emerge in the confined chalcogenide system. Although it is still not well understood how the nano-confinement affects such changes in the magnetic properties, the unique confinement effects seem to be the contributing factors to the novel generation

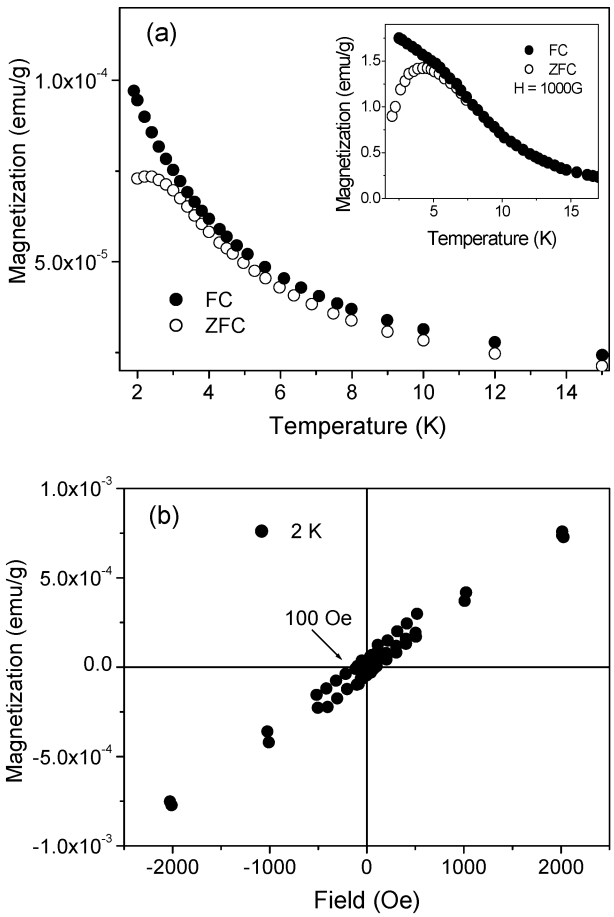

Fig. 7. (a) Temperature-dependent FC (closed circle) and ZFC (open circle) DC magnetic susceptibilities at the field of 1000 G and (b) hysteresis loop for the CST@AlMCM nanocomposite at 2 K. The inset is the temperature-dependent FC (closed circle) and ZFC (open circle) DC magnetic susceptibilities for the amorphous bulk $Co_3(SbTe_3)_2$.

of the superparamagnetic domain (spin-ordered system) and the weak remanent magnetization of the FC curve which exists well above the blocking temperature for the confined magneto-semiconductor within the long-range ordered nanochannels.

CONCLUSIONS

Optically and magnetically interesting ternary chalcogenide was incorporated within the mesoporous AlMCM-41 nanochannels. The resulting nanocomposite including the ternary chalcogenide presented increased crystallographic ordering within the long-range ordered nanochannels. The excitation and the emission spectra showed both the size and energy quantization effects for the confined chalcogenide within the nanochannels. Moreover, the spatial confinement induced the suppression of the optical phonon coupling to the photoexcited carriers, which resulted in the occurrence of the band-edge emission in the confined chalcogenide system. In addition, as the spin-glass chalcogenide is incorporated within the nanochannels, the superparamagnetic phase is newly observed. Such ordered spin coupling is possibly induced by the confinement effects such as enhanced crystallinity, size and energy quantization, and reduced thermal effect.

ACKNOWLEDGMENTS

This work was financially supported by a National Research Laboratory (grant No. M1-0302-00-0027) program. We are grateful for the instrumental support from the equipment facility of CRM-KOSEF and the PL decay measurement to Dr. I.-W. Hwang. Prof. J.-S. Jung is thankful for a grant (Myongji RRC).

Received April 20, 2005.

REFERENCES

1. Hulteen, J. C.; Martin, C. R. *J. Mater. Chem*. **1997**, *7*, 1075.
2. Trau, M.; Yao, N.; Kim, E.; Xia, Y.; Whitesides, G. M.; Aksay, I. A. *Nature* **1997**, *390*, 674.
3. Yang, P.; Deng, T.; Zhao, D.; Feng, P.; Pine, D.; Chmelka, B. F.; Whitesides, G. M.; Stucky, G. D. *Science* **1998**, *282*, 2244.
4. Jung, J.-S.; Chae, W.-S.; McIntyre, R. A.; Seip, C. T.; Wiley, J. B.; O'Connor, C. J. *Mater. Res. Bull* **1999**, *34*, 1353.
5. Parala, H.; Winkler, H.; Kolbe, M.; Wohlfart, A.; Fischer, R. A.; Schmechel, R.; Seggern, H. *Adv. Mater.* **2000**, *12*, 1050.
6. Han, Y.-J.; Kim, J. M.; Stucky, G. D. *Chem. Mater.* **2000**, *12*, 2068.
7. Huang, M. H.; Choudrey, A.; Yang, P. *Chem. Commun*. **2000**, 1063.
8. Zhang, W.-H.; Shi, J.-L.; Chen, H.-R.; Hua, Z.-L.; Yan, D.-S. *Chem. Mater.* **2001**, *13*, 648.
9. Shin, H. J.; Ryoo, R.; Liu, Z.; Terasaki, O. *J. Am. Chem. Soc*. **2001**, *123*, 1246.
10. Wang, D.; Luo, H.; Kou, R.; Gil, M. P.; Xiao, S.; Golub, V. O.; Yang, Z.; Brinker, C. J.; Lu, Y. *Angew. Chem., Int. Ed*. **2004**, *43*, 6169.
11. Kruk, M.; Jaroniec, M.; Sakamoto, Y.; Terasaki, O.; Ryoo, R.; Ko, C. H. *J. Phys. Chem. B* **2000**, *104*, 292.
12. Zhao, D.; Feng, J.; Huo, Q.; Melosh, N.; Fredrickson, G. H.; Chmelka, B. F.; Stucky, G. D. *Science* **1998**, *279*, 548.
13. Kim, J. M.; Kwak, J. H.; Jun, S.; Ryoo, R. *J. Phys. Chem*. **1995**, *99*, 16742.
14. Shen, S.; Tian, B.; Yu, C.; Xie, S.; Zhang, Z.; Tu, B.; Zhao, D. *Chem. Mater.* **2003**, *15*, 4046.
15. Braun, P. V.; Osenar, P.; Stupp, S. I. *Nature* **1996**, *380*, 325.
16. MacLachlan, M. J.; Coombs, N.; Ozin, G. A. *Nature* **1999**, *397*, 681.
17. Trikalitis, P. N.; Kasthuri Rangan, K.; Bakas, T.; Kanatzidis, M. G. *Nature* **2001**, *410*, 671.
18. Ryoo, R.; Ko, C. H.; Cho, S. J.; Kim, J. M. *J. Phys. Chem. B* **1997**, *101*, 10610.
19. Liu, N.; Assink, R. A.; Brinker, C. J. *Chem. Commun*. **2003**, 370.
20. Nooney, R. I.; Thirunavukkarasu, D.; Chen, Y.; Josephs, R.; Ostafin, A. E. *Chem. Mater.* **2002**, *14*, 4721.
21. Yu, C.; Fan, J.; Tian, B.; Zhao, D.; Stucky, G. D. *Adv. Mater.* **2002**, *14*, 1742.
22. Chae, W.-S.; Lee, S.-W.; Im, S.-J.; Moon, S.-W.; Zin, W.-C.; Lee, J.-K.; Kim, Y.-R. *Chem. Commun*. **2004**, 2554.
23. Wu, Y.; Cheng, G.; Katsov, K.; Sides, S. W.; Wang, J.; Tang, J.; Fredrickson, G. H.; Moskovits, M.; Stucky, G. D. *Nature Mater.* **2004**, *3*, 816.
24. Srdanov, V. I.; Alxneit, I.; Stucky, G. D.; Reaves, D. M.; DenBaars, S. P. *J. Phys. Chem. B* **1998**, *102*, 3341.
25. Hirai, T.; Okubo, H.; Komasawa, I. *J. Phys. Chem. B* **1999**, *103*, 4228.
26. Besson, S.; Gacoin, T.; Ricolleau, C.; Boilot, J.-P. *Chem. Commun*. **2003**, 360.
27. Jung, J.-S.; Choi, K.-H.; Chae, W.-S.; Kim, Y.-R.; Jun, J.-H.; Malkinski, L.; Kodenkandath, T.; Zhou, W.; Wiley, J. B.; O'Connor, C. J. *J. Phys. Chem. Solids* **2003**, *64*, 385.

28. Brieler, F. J.; Fröba, M.; Chen, L.; Klar, P. J.; Heimbrodt, W.; Nidda, H.-A. K.; Loidl, A. *Chem. Eur. J*. **2002**, *8*, 185.
29. Pattantyus-Abraham, A. G.; Wolf, M. O. *Chem. Mater.* **2004**, *16*, 2180.
30. Xu, W.; Guo, H.; Akins, D. L. *J. Phys. Chem. B* **2001**, *105*, 1543.
31. Molenkamp, W. C.; Watanabe, M.; Miyata, H.; Tolbert, S. H. *J. Am. Chem. Soc*. **2004**, *126*, 4476.
32. Chae, W.-S.; Ko, J.-H.; Hwang, I.-W.; Kim, Y.-R. *Chem. Phys. Lett*. **2002**, *365*, 49.
33. Chae, W.-S.; Yoon, J.-H.; Yu, H.; Jang, D.-J.; Kim, Y.-R. *J. Phys. Chem. B* **2004**, *108*, 11509.
34. O'Connor, C. J.; Jung, J.-S.; Zhang, J. H. *Chemistry, Structure, and Bonding of Zintl Phases and Ions*; Kauzlarich, S. M., Ed.; VCH Publisher: New York, 1996; Chap. 7.
35. Jung, J.-S.; Wu, B.; Ren, L.; Tang, J.; Ferre, J.; Jamet, J.; O'Connor, C. J. *J. Mater. Res*. **1994**, *9*, 909.
36. Jung, J.-S.; Wu, B.; Stevens, E. D.; O'Connor, C. J. *J. Solid State Chem*. **1991**, *94*, 362.
37. Jung, J.-S.; Kim, J.-Y.; Chae, W.-S.; Kim, Y.-R.; Jun, J.-H.; Malkinski, L.; Zhou, W.; Kumbhar, A.; Viciu, M. L.; Wiley, J. B.; O'Connor, C. J. *Mat. Res. Soc. Symp. Proc*. **2002**, Vol. 676, Y3.45.
38. Chae, W.-S.; Hwang, I.-W.; Jung, J.-S.; Kim, Y.-R. *Chem. Phys. Lett*. **2001**, *341*, 279.
39. Hwang, I.-W.; Choi, H.-H.; Cho, B.-K.; Lee, M.; Kim, Y.-R. *Chem. Phys. Lett*. **2000**, *325*, 219.
40. O'Connor, C. J. *Prog. Inor. Chem*. **1982**, *29*, 203.
41. Anderson, P. W. *Nature (London) Phys. Sci*. **1972**, *235*, 163.
42. Brodsky, M. H. *Amorphous Semiconductors*; Springer-Verlag: New York, 1979.
43. Chen, W.; Wang, Z. G.; Lin, Z. J.; Lin, L. Y. *J. Appl. Phys*. **1997**, *82*, 3111.
44. Chae, W.-S.; Kim, Y.-R.; Jung, J.-S. *J. Phys. Chem. B* **2003**, *107*, 1585.
45. Bawendi, M. G.; Carroll, P. J.; Wilson, W. L.; Brus, L. E. *J. Chem. Phys*. **1992**, *96*, 946.
46. Ramvall, P.; Tanaka, S.; Nomura, S.; Riblet, P.; Aoyagi, Y. *Appl. Phys. Lett*. **1999**, *75*, 1935.
47. Bockelmann, U.; Egeler, T. *Phys. Rev. B* **1992**, *46*, 15574.
48. Efros, A. L.; Kharchenko, V. A.; Rosen, M. *Solid State Commun*. **1995**, *93*, 281.
49. Leslie-Pelecky, D. L.; Rieke, R. D. *Chem. Mater.* **1996**, *8*, 1770.
50. Hou, Y.; Kondoh, H.; Kogure, T.; Ohta, T. *Chem. Mater.* **2004**, *16*, 5149.
51. Kommareddi, N. S.; Tata, M.; John, V. T.; McPherson, G. L.; Herman, M. F.; Lee, Y.-S.; O'Connor, C. J.; Akkara, J. A.; Kaplan, D. L. *Chem. Mater.* **1996**, *8*, 801.
52. Dormann, J. L.; Cherkaoui, R.; Spinu, L.; Noguès, M.; Lucari, F.; D'Orazio, F.; Fiorani, D.; Garcia, A.; Tronc, E.; Jolivet, J. P. *J. Magn. Magn. Mater.* **1998**, *187*, L139.